Inorganic Chemistry
Article
pubs.acs.org/IC

Expanding the Ruddlesden−Popper Manganite Family: The *n* = 3 $La_{3.2}Ba_{0.8}Mn_3O_{10}$ Member

Joke Hadermann,*[,†] Artem M. Abakumov,[†,§] Alexander A. Tsirlin,[‡,⊥] Marina G. Rozova,[§] Eleni Sarakinou,[†,∥] and Evgeny V. Antipov[§]

[†]EMAT, University of Antwerp, Groenenborgerlaan 171, 2020 Antwerp, Belgium
[‡]Max Planck Institute for Chemical Physics of Solids, Nöthnitzer Str. 40, 01187 Dresden, Germany
[§]Department of Chemistry, Moscow State University, 119991 Moscow, Russia
[∥]Physics Department, Aristotle University of Thessaloniki, 54124, Thessaloniki Greece
[⊥]National Institute of Chemical Physics and Biophysics, 12618 Tallinn Estonia

Supporting Information

ABSTRACT: $La_{3.2}Ba_{0.8}Mn_3O_{10}$, a representative of the rare *n* = 3 members of the Ruddlesden−Popper manganites $A_{n+1}Mn_nO_{3n+1}$, was synthesized in an evacuated sealed silica tube. Its crystal structure was refined from a combination of powder X-ray diffraction (PXD) and precession electron diffraction (PED) data, with the rotations of the MnO_6 octahedra described within the symmetry-adapted mode approach (space group *Cccm*, a = 29.068(1) Å, b = 5.5504(5) Å, c = 5.5412(5) Å; PXD R_F = 0.053, R_P = 0.026; PED R_F = 0.248). The perovskite block in $La_{3.2}Ba_{0.8}Mn_3O_{10}$ features an octahedral tilting distortion with out-of-phase rotations of the MnO_6 octahedra according to the (Φ,Φ,0)(Φ,Φ,0) mode, observed for the first time in the *n* = 3 Ruddlesden−Popper structures. The MnO_6 octahedra demonstrate a noticeable deformation with the elongation of two apical Mn−O bonds due to the Jahn−Teller effect in the Mn^{3+} cations. The relationships between the octahedral tilting distortion, the ionic radii of the cations at the A- and B-positions, and the mismatch between the perovskite and rock-salt blocks of the Ruddlesden−Popper structure are discussed. At low temperatures, $La_{3.2}Ba_{0.8}Mn_3O_{10}$ reveals a sizable remnant magnetization of about 1.3 μ_B/Mn at 2 K, and shows signatures of spin freezing below 150 K.

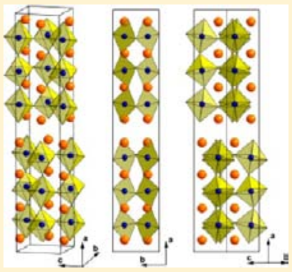

INTRODUCTION

Ruddlesden−Popper (RP) manganites $A_{n+1}Mn_nO_{3n+1}$ are presently of interest because of the rich physics related to their intrinsic low-dimensional nature and the presence of Mn cations in different oxidation states. For example, the effect of tunnelling colossal magnetoresistance observed in the *n* = 2 $La_{1.2}Sr_{1.8}Mn_2O_7$ compound is of particular importance.[1] The RP homologues can be considered as intergrowth structures with alternating ($A_{n-1}B_nO_{3n-1}$) perovskite-type blocks and (A_2O_2) rock-salt-type blocks. The perovskite blocks have a thickness of *n* BO_6 octahedra, where *n* is the homologue number. The variation of *n* enables investigating the dependence of the physical properties on the “dimensionality” of the electronic system starting from the “two-dimensional” *n* = 1 A_2MnO_4 structure (A = Ca, Sr, rare earth) with a single layer of MnO_6 octahedra up to the three-dimensional framework in $n = \infty$ $AMnO_3$ perovskites. However, the preparation of the RP homologues becomes enormously difficult for large *n*, because the energy differences between the subsequent homologues decrease with *n*, thus causing a high concentration of stacking faults (intergrowths of the homologues with different *n*). Only a small number of *n* = 3 RP manganites have so far been synthesized in bulk form. Many of those feature a mixture of different transition-metal cations on the B-site, for example, $Sr_4Mn_{3-x}Fe_xO_{10-\delta}$,[2] $Ca_4Mn_2TiO_{9.93}$,[3] $Na_2Ln_2Ti_{3-x}Mn_xO_{10}$ (Ln = Sm, Eu, Gd, and Dy; $0 \leq x \leq 1$),[4] $Ca_4Mn_{3-x}Ta_xO_{10}$ ($0 \leq x \leq 0.3$).[5] The purely manganese-based *n* = 3 RP compounds are few: only $Ca_4Mn_3O_{10}$[6] and the mixed A-site compound $Bi_xCa_{4-x}Mn_3O_{10}$.[7] All these manganites feature Mn atoms with the oxidation state close to +4, whereas the reduction toward Mn^{3+}, which is essential for the colossal magnetoresistance, remains a challenging problem.

In this Article we report the synthesis, structure determination, and magnetic properties of $La_{3.2}Ba_{0.8}Mn_3O_{10}$, the *n* = 3 member of the RP series $(La,Ba)_{n+1}Mn_nO_{3n+1}$ with the Mn oxidation state close to +3. In order to determine properly the octahedral tilting distortion in the pseudotetragonal $La_{3.2}Ba_{0.8}Mn_3O_{10}$, we applied the original technique based on a joint structure refinement from a combination of powder X-ray diffraction and precession electron diffraction data while determining the rotations of the MnO_6 octahedra with a symmetry-adapted mode approach.

EXPERIMENTAL SECTION

The sample with the bulk composition $La_4BaMn_5O_{13}$ was prepared from a mixture of La_2O_3, BaO, Mn_2O_3, and MnO. La_2O_3 was dried by annealing at 900 °C for 12 h in air. BaO was obtained by thermal

Received: June 22, 2012
Published: October 17, 2012

dx.doi.org/10.1021/ic301332e | *Inorg. Chem.* 2012, 51, 11487−11492

decomposition of $BaCO_3$ at 1100 °C for 36 h in a dynamic vacuum of 10^{-4} mbar. All the materials were ground in an Ar-filled glovebox, pressed into pellets, placed into an alumina crucible, and sealed into an evacuated silica tube. The tube was annealed at 1000 °C for 150 h and furnace-cooled.

Phase analysis of the samples was performed with powder X-ray diffraction (PXD) data collected on a Huber G670 Guinier diffractometer (Cu Kα1 radiation). PXD data for the Rietveld refinement were obtained with a STOE STADI-P diffractometer (Cu Kα1 radiation, transmission geometry, Ge(111) monochromator, linear PSD).

The samples for transmission electron microscopy (TEM) were made by crushing the powder in ethanol and depositing the suspension on a copper grid covered with a holey carbon film. Selected area electron diffraction (SAED) patterns and precession electron diffraction (PED) patterns were taken on a Philips CM20 microscope equipped with a Spinning Star precession module. Energy dispersive X-ray (EDX) spectra were taken simultaneously with the ED patterns using the Oxford Instruments EDX attachment. The PED patterns were taken on CCD, with a precession angle of 2.5°. The intensities were extracted and treated using the Calidris software ELD and Triple. High resolution transmission electron microscopy (HRTEM) images were taken on a JEOL 4000EX microscope.

Structure refinement from combined PXD and PED data was performed with JANA2006.[8] Analysis of the electron diffraction patterns was done using the commercial software packages JEMS and CrystalKit.

Magnetic susceptibility was measured with Quantum Design SQUID MPMS in the temperature range 2−380 K in fields up to 5 T in both field-cooling and zero-field-cooling regimes.

Structure Determination. The PXD pattern of the as-prepared sample demonstrated the presence of a compound with a perovskite-based layered structure as the main phase. The reflections of this phase were indexed on a body-centered tetragonal unit cell with the unit cell parameters a_t = 3.9200(1) Å, c_t = 29.064(1) Å. The lattice parameters and intensity distribution for the reflections on the PXD pattern evidence that this phase has the n = 3 structure of the $A_{n+1}B_nO_{3n+1}$ RP series and, consequently, the chemical composition $(La,Ba)_4Mn_3O_{10}$. EDX analyses provided a La/Ba ratio of 4.1(5). No substantial deviations were found in EDX measurements between different areas on the crystallites, or between different crystallites. The main phase can therefore be noted as $La_{3.2}Ba_{0.8}Mn_3O_{10}$. The admixture phases in the sample were identified as MnO and La_2O_3. Repeated attempts to vary the chemical composition and/or annealing temperature were unsuccessful and did not allow us to prepare a single-phase sample of $La_{3.2}Ba_{0.8}Mn_3O_{10}$ or reduce the amount of the admixture phases.

The Rietveld refinement of the simplest $I4/mmm$ n = 3 RP structure against the PXD data readily provided a reasonable fit (R_F = 0.062, R_P = 0.025). However, the atomic displacement parameters for the oxygen atoms were unacceptably large (U_{iso} = 0.055 Å^2). Decreasing the occupancy of the oxygen positions does not account for this large ADP; hence, a structure distortion should be expected. A cooperative octahedral tilting within the perovskite blocks of the RP structure is a plausible reason for this distortion. To check this possibility further, we verified the unit cell and space symmetry of $La_{3.2}Ba_{0.8}Mn_3O_{10}$ with transmission electron microscopy.

Series of SAED patterns were obtained by rotating the crystal around different axes and recording the SAED pattern of each encountered zone. These were combined with Fourier transforms (FT) taken from the HRTEM images along different main zones. On the basis of the whole series of SAED patterns and Fourier transforms, the reciprocal lattice was reconstructed and could be indexed using the following approximate cell parameters: $a \approx 29$ Å, $b \approx c \approx 5.6$ Å ($=a_p\sqrt{2}$) (a_p is the cell parameter of the perovskite structure).

Figure 1 shows the most important ED patterns of the series. The [010]/[001] ED pattern is an overlap of the patterns of the zones [010] and [001]. The [010] and [001] ED patterns were never obtained separately; the reason for this is clarified by Figure 2. Figure 2 shows an HRTEM image (and corresponding FTs) of a twinned area consisting of the [010]- and [001]-oriented domains. The FT of the [001] domain clearly differs from that of the [010] domain by the presence of the $hk0$: $h + k = 2n$ reflections. The reflection conditions $hk0$: $h + k = 2n$ and $h0l$: $h,l = 2n$ were derived from these FTs.

The [011] HRTEM image (Figure 3) demonstrates that crystallites with a large amount of stacking faults exist. The intergrowths in Figure 3 can be explained as lower members of the RP series. By analogy with other RP structures, the zigzag rows of brightest dots correspond to the rock salt (RS) block (A_2O_2) (the position of these layers is also

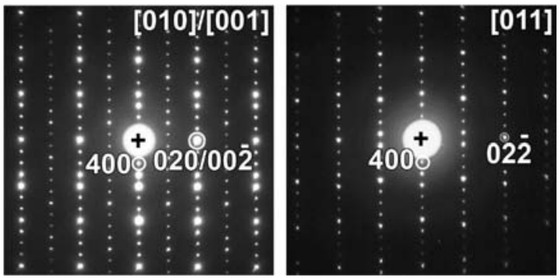

Figure 1. Electron diffraction patterns of $La_{3.2}Ba_{0.8}Mn_3O_{10}$ along the directions [010], [010] + [001], and [011].

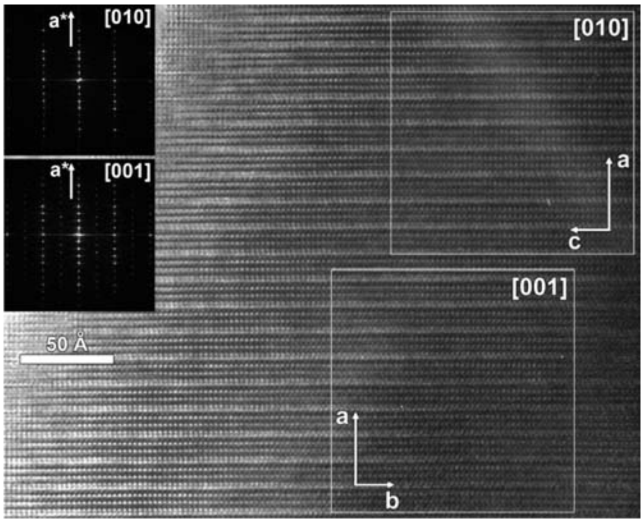

Figure 2. High resolution electron microscopy image along [010] and [001] as twinned domains next to each other. The Fourier transforms of the two areas confirm their correspondence to each twinned domain.

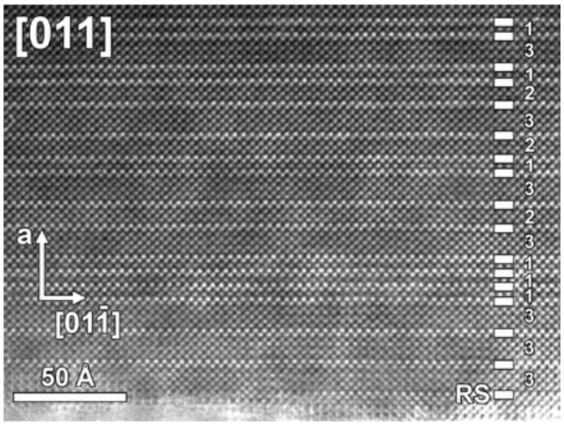

Figure 3. HRTEM image along [011] showing the presence of intergrowths of n = 1 and n = 2 RP slabs within the n = 3 RP main phase.

indicated by a white dash at the right side of the image). The number of layers in between two such RS blocks in Figure 3 varies from 1 to 3 to 5, corresponding, respectively, to a slab of $n = 1$ RP, $n = 2$ RP, and the main phase with $n = 3$ RP. The occurrence of such intergrowths of other members is common in RP compounds. Crystallites without stacking faults have also been observed (Figure 4). A large degree of stacking disorder makes the identification of the reflection conditions ambiguous when the structure is viewed along the *a*-axis because the slabs with different *n* are projected on to each other. To overcome this problem, the 0*kl* reflection condition has been derived from the analysis of all 0*kl* reflections and extinctions obtained from the different other zones in the series and has been found to undubiously be 0*kl*: $k,l = 2n$. The reflection condition *hkl*: $h + k = 2n$ is also valid for all patterns. These reflection conditions correspond to the extinction symbol *Ccc*-, leaving two possible space groups, *Ccc*2 and *Cccm*.

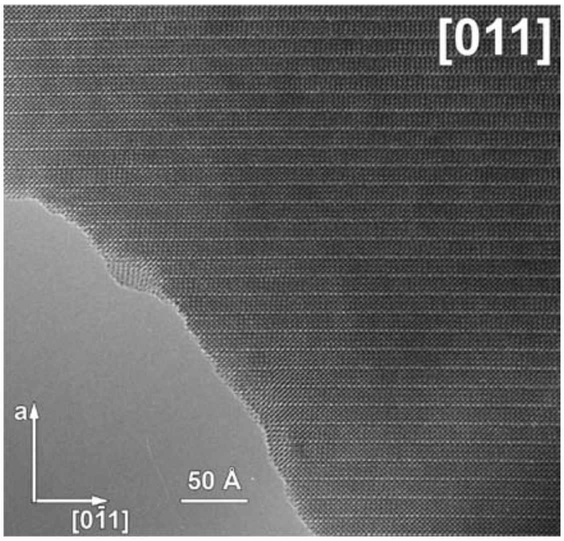

Figure 4. High resolution electron microscopy overview image along [011] of a crystal free from stacking faults.

To the best of our knowledge, no $n = 3$ RP compounds with the space group *Cccm* were reported in literature. The structure of the $n = 3$ compound without the octahedral tilting has a tetragonal unit cell with $a_t = b_t = a_p \approx 3.9$ Å and the space group *I*4/*mmm*. The list of theoretically possible space groups and the respective tilt systems does include the distortion consistent with the *Cccm* space group.[9] This tilt system is (Φ,Φ,0)(Φ,Φ,0) in the notation used by Aleksandrov et al.[9] (a^-a^-0/a^-a^-0 in Glazer's notations). In this tilt system, the octahedra are rotated around the *a* and *b* axes of the parent tetragonal *I*4/*mmm* structure, with an antiphase relation between the neighboring layers and between the neighboring perovskite blocks. Being transformed into the orthorhombic $a = c_t$, $b \approx c \approx a_t\sqrt{2}$ *Cccm* supercell, this comes down to a rotation of the octahedra around the *c*-axis only.

The *hkl*: $k + l \neq 2n$ superlattice reflections arising from the octahedral tilt are too weak to be detected on the PXD pattern. Therefore, we used a combination of the PXD data and precession electron diffraction (PED) data to refine the $La_{3.2}Ba_{0.8}Mn_3O_{10}$ structure taking into account the octahedral tilt. The PED patterns were taken along different zone-axes intentionally avoiding the main zones (i.e., [100], [010], [110], etc.) as they are most affected by dynamical diffraction effects. They were taken from as thin as possible crystals, as could be judged by eye. The obtained PED patterns are shown in the Supporting Information Figures S4–S7. The extraction of the intensities and the data reduction are described in detail in the Supporting Information. Among the reflections from the basic *I*4/*mmm* structure, the intensities of 31 superlattice reflections were measured and used in a subsequent refinement.

In order to minimize the amount of refineable parameters, we have employed the symmetry-adapted mode approach.[10,11] The *Cccm* structure, being viewed as a distorted variant of the parent *I*4/*mmm* structure, can be represented as a set of distortion modes given by irreducible representations (irreps) of the parent *I*4/*mmm* space group. The amplitudes of the distortions are then used as refineable parameters instead of the conventional atomic coordinates. One can expect that the distortion mode associated with the octahedral rotation will be the primary distortion component giving the main impact to the intensities of the superlattice reflections.

The symmetry analysis was performed with the ISODISPLACE program.[12] For the **k**-vector ($^1/_2$,$^1/_2$,0), the (Φ,Φ,0)(Φ,Φ,0) octahedral tilt is governed by the X_4^+ irrep of the *I*4/*mmm* space group, leading to the symmetry reduction to *Cccm* with the transformation matrix (0,0,1), (1,1,0), (−1,1,0) for the supercell. The displacements of the equatorial oxygen atoms of the MnO_6 octahedra are given by the symmetry modes $X_4^+(a,a)B_{1u}(a)$ (for the octahedra at the center of the perovskite block) and $X_4^+(a,a)A_1(a)$ (for the octahedra at the periphery of the perovskite block); those displacement parameters were set to be equal in the refinement (see ref 10 for notations). The apical oxygen atoms displace according to the $X_4^+(a,a)E(a)$ mode. The restrictions on the atomic coordinates of the oxygen atoms imposed by the symmetry modes were introduced to the JANA2006 program as a set of linear constraints.

While the symmetry-adapted modes were used to describe the displacements of the oxygen atoms, the atomic coordinates of the cations were refined in a conventional way. The A-positions were assumed to be randomly occupied by the La and Ba cations in a 4:1 ratio, according to the EDX analysis. The overall isotropic ADP was refined for all atoms. The admixture phases MnO and La_2O_3 were also introduced into the Rietveld refinement. The quantities of these phases were refined to 9.0(3) wt % and 1.3(1) wt %, respectively. Considering the bulk composition of the specimen $La_4BaMn_5O_{13}$, the composition of the RP phase can be calculated from the weight fractions of the admixture phases as "$La_{3.34}Ba_{0.85}Mn_{3.00}O_{9.73}$" that is very close to the nominal composition $La_{3.2}Ba_{0.8}Mn_3O_{10}$. The crystallographic parameters, atomic coordinates, and main interatomic distances are given in Tables 1, 2, and 3, respectively. The experimental, calculated, and difference PXD profiles along with the observed and calculated PED structure amplitudes are shown in Figure 5. The crystal structure of $La_{3.2}Ba_{0.8}Mn_3O_{10}$ is shown in Figure 6.

Table 1. Selected Parameters from the Joint PED and XRD Rietveld Refinements for $La_{3.2}Ba_{0.8}Mn_3O_{10}$

composition	$La_{3.2}Ba_{0.8}Mn_3O_{10}$
space group	*Cccm*
a, Å	29.068(1)
b, Å	5.5504(5)
c, Å	5.5412(5)
Z	4
cell volume, Å^3	894.00(9)
calcd density, g/cm^3	6.530
overall U_{iso}, Å^2	0.0118(7)
params refined	38
radiation (X-rays)	Cu Kα1, $\lambda = 1.5406$ Å
2θ range and step, deg	$4 \leq 2\theta \leq 100$; 0.02
R_F, R_P, R_{wP}	0.053, 0.026, 0.036
radiation (PED)	electrons, $\lambda = 0.025$ Å
no. reflns	161
R_F	0.248

Magnetic Properties. The magnetic susceptibility (χ) was measured on the powder sample containing 9.0(3) wt % of MnO and 1.3(1) wt % of La_2O_3. Both impurities do not influence any of the results presented below, because La_2O_3 is diamagnetic, whereas MnO undergoes an antiferromagnetic transition around 120 K and only weakly contributes to the sample magnetization. According to ref 13 the susceptibility of MnO is below 0.005 emu/mol, which is 2 orders

Table 2. Positional Parameters for $La_{3.2}Ba_{0.8}Mn_3O_{10}$

atom	x/a	y/b	z/c
LaBa1^a	0.5488(1)	0.2496(6)	0
LaBa2^a	0.6805(1)	0.2463(6)	0
Mn1	1/4	1/4	0
Mn2	0.3901(3)	0.254(1)	0
O1	0.7393(4)	0	1/4
O2	0.3187(2)	0.322(2)	0
O3	0.9014(4)	0	1/4
O4	0.6200(4)	0	1/4
O5	0.4650(4)	0.178(2)	0

$^a g$ = 0.8La + 0.2Ba.

Table 3. Main Interatomic Distances (Å) for $La_{3.2}Ba_{0.8}Mn_3O_{10}$

LaBa1−O3	2.439(8) × 2	LaBa2−O1	2.591(9) × 2
LaBa1−O4	2.85(1) × 2	LaBa2−O1	3.06(1) × 2
LaBa1−O5	2.47(1) × 1	LaBa2−O2	2.40(1) × 1
LaBa1−O5	2.41(1) × 1	LaBa2−O2	2.802(2) × 2
LaBa1−O5	2.827(2) × 2	LaBa2−O2	3.15(1) × 1
		LaBa2−O3	3.09(1) × 2
Mn1−O1	1.985(2) × 4	LaBa2−O4	2.624(9) × 2
Mn1−O2	2.036(6) × 2	Mn2−O2	2.108(9) × 1
		Mn2−O3	1.972(5) × 2
		Mn2−O4	1.998(5) × 2
		Mn2−O5	2.22(1) × 1

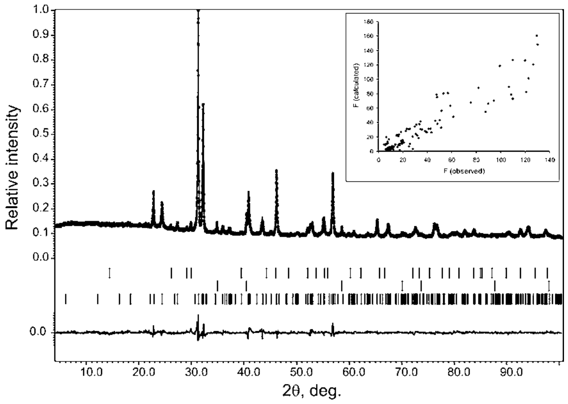

Figure 5. Experimental, calculated, and difference PXD patterns of $La_{3.2}Ba_{0.8}Mn_3O_{10}$. The bars mark the reflection positions for La_2O_3 (top row), MnO (middle row), and $La_{3.2}Ba_{0.8}Mn_3O_{10}$ (bottom row). The insert shows F(observed) − F(calculated) structure amplitudes plot for the PED data for $La_{3.2}Ba_{0.8}Mn_3O_{10}$.

of magnitude lower than the susceptibility of $La_{3.2}Ba_{0.8}Mn_3O_{10}$ (Figure 7).

Above 250−300 K, the inverse susceptibility ($1/\chi$) is linear and follows the Curie−Weiss law $\chi = C/(T + \theta)$ with the Curie constant C = 4.50 emu K/mol and the Curie−Weiss temperature $\theta = -150$ K (Figure 7). The experimental Curie constant yields the effective magnetic moment of about 6.0 μ_B, which exceeds the spin-only moment of 4.9 μ_B for Mn^{3+} as the spin-2 cation. We note, however, that the estimate of the effective moment is not precise, because the experimental data were not corrected for the MnO impurity. Additionally, the 300−380 K temperature range may be too narrow to extract precise parameters. Nevertheless, the negative θ value is robust with respect to these uncertainties and indicates predominantly ferromagnetic exchange couplings.

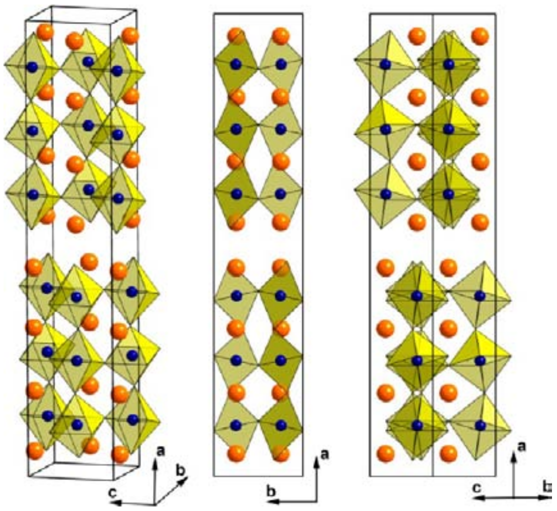

Figure 6. Crystal structure of $La_{3.2}Ba_{0.8}Mn_3O_{10}$: clinographic viewing (left), [001] projection (middle), and [011] projection (right). The Mn and LaBa atoms are shown as blue and orange spheres, respectively.

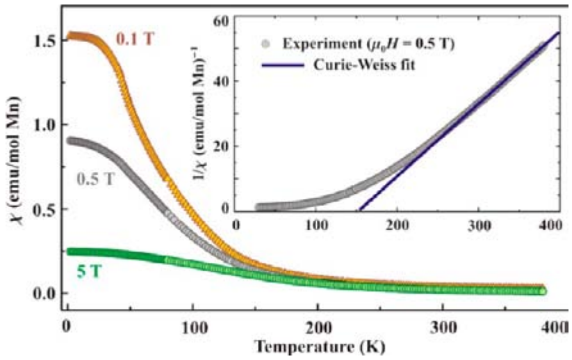

Figure 7. Magnetic susceptibility of $La_{3.2}Ba_{0.8}Mn_3O_{10}$ measured in applied fields of 0.1, 0.5, and 5 T. The inset shows the Curie−Weiss fit to the data above 300 K.

Below 200 K, the susceptibility of $La_{3.2}Ba_{0.8}Mn_3O_{10}$ rapidly increases. The magnetization (M vs H) curve develops a hysteresis with a remnant magnetization (M_r) of about 1.3 μ_B/Mn at 2 K (Figure 8). This value is close to one-third of the maximum magnetization of 4 μ_B expected for Mn^{3+} with four unpaired electrons. Therefore, the ferromagnetic signal is intrinsic and cannot be ascribed to, e.g., intergrowths that may produce weak ferromagnetic moments on the order of 0.01 μ_B/Mn.[14]

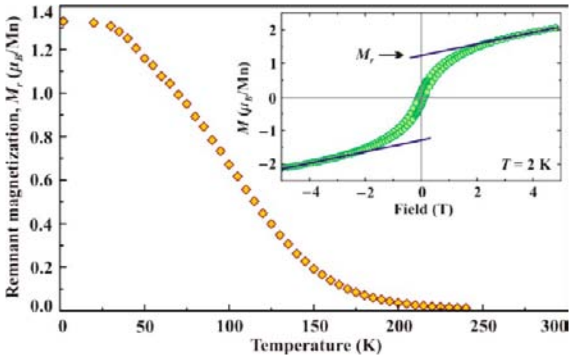

Figure 8. Temperature dependence of the remnant magnetization (M_r). The inset shows the magnetization loop measured at 2 K, and the estimate of M_r from the linear fit between 3.5 and 5 T.

Although reminiscent of the ferrimagnetic order, the remnant magnetization does not appear abruptly and rather shows a continuous temperature evolution without a well-defined transition temperature. To track temperature dependence of M_r, we measured the magnetization loops at different temperatures and fitted the linear part of the $M(H)$ curves between 3.5 and 5 T. The remnant magnetization continuously decreases upon heating and vanishes above 200 K (Figure 8).

Comparative measurements in field-cooling (FC) and zero-field-cooling (ZFC) regimes show the divergence of the low-field FC and ZFC susceptibility curves below 150 K (Figure 9). Although this divergence is a typical signature of spin freezing, $La_{3.2}Ba_{0.8}Mn_3O_{10}$ does not form a perfect spin glass. The magnetic field of about 1 T destroys random spin arrangement and produces the large magnetization of 1.3 μ_B/Mn at 2 K (Figure 8).

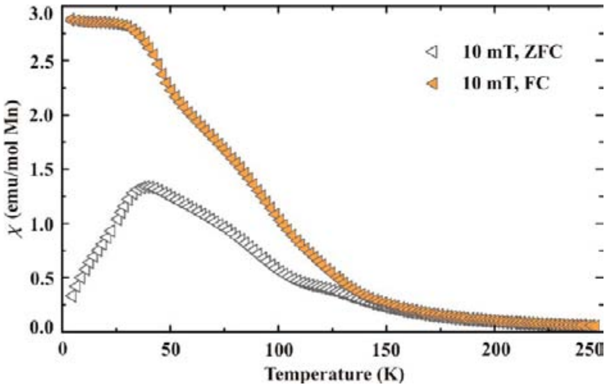

Figure 9. Magnetic susceptibility of $La_{3.2}Ba_{0.8}Mn_3O_{10}$ measured in field-cooled (FC, filled symbols) and zero-field-cooled (ZFC, open symbols) regimes in the applied field of 10 mT.

Altogether, our results suggest that $La_{3.2}Ba_{0.8}Mn_3O_{10}$ combines the features of spin glass and ferrimagnet. The magnetic transition around 150 K is accompanied by the formation of large remnant magnetization and partial spin freezing. This scenario is not unusual for mixed-valence manganites that are prone to spin freezing and magnetic phase separation because of a subtle competition between antiferromagnetic superexchange and ferromagnetic double exchange.[15] Further work on the low-temperature magnetism of $La_{3.2}Ba_{0.8}Mn_3O_{10}$ is clearly desirable. For example, neutron-diffraction experiments should access the putative magnetic order below 150 K, whereas muon spin rotation and nuclear magnetic resonance could provide further insight into the spin dynamics and spin freezing.

■ DISCUSSION

According to the chemical composition $La_{3.2}Ba_{0.8}Mn_3O_{10}$, the formal Mn oxidation state is very close to +3 (+2.93). Assuming a random distribution of the La and Ba cations over the A-positions in the (A_2O_2) rock-salt layers and in the perovskite blocks, the tolerance factor for the perovskite block is $t = 0.96$. Although this is close to unity, it favors the occurrence of an octahedral tilting distortion for eliminating the mismatch between the A−O and Mn−O interatomic distances. Apparently, the mismatch between the rock-salt (A_2O_2) block and the perovskite block also contributes to the tilting distortion. In $La_{3.2}Ba_{0.8}Mn_3O_{10}$, the in-plane dimension of the rock-salt subcell of the (A_2O_2) block is $a_{RS} = 5.546$ Å. This is noticeably larger than the corresponding parameter in other RP transition metal oxides with similar chemical composition of the rock-salt block. For example, in $La_{1.8}Ba_{0.2}CuO_4$[16] and $La_{1.52}Ba_{0.48}NiO_4$[17] these parameters are equal to $a_{RS} = 5.375$ and 5.452 Å, respectively. This indicates that the rock-salt block in $La_{3.2}Ba_{0.8}Mn_3O_{10}$ is under tensile strain, whereas the perovskite block is subjected to a compressive strain. Therefore, the tilting distortion is essential to relieve the compressive strain in the perovskite block and facilitate the formation of the intergrowth RP-type structure.

The coupling between the tilting distortion of the perovskite block and the size mismatch between the rock-salt and perovskite slabs is additionally corroborated by the structural investigations on the $n = 2$ RP reduced $La_{1.25}Ba_{1.75}Mn_2O_6$ and oxidized $La_{1.25}Ba_{1.75}Mn_2O_7$ phases.[18] Both compounds demonstrate the large in-plane parameter of the rock-salt layer ($a_{RS} = 5.670$ and 5.581 Å, respectively), but their crystal structures were refined from neutron powder diffraction data in the *I*4/*mmm* space group that excludes any octahedral tilting. The peculiarity of these phases is the A-site ordering. In the reduced $La_{1.25}Ba_{1.75}Mn_2O_6$ phase, all Ba^{2+} cations are located at the rock-salt block, whereas the La^{3+} cations occupy positions between the (MnO_2) layers in the perovskite block. This A-site ordering is apparently promoted by the ordering of oxygen vacancies, which are concentrated in the (La□) layers (□ = oxygen vacancy). A gentle oxidation of $La_{1.25}Ba_{1.75}Mn_2O_6$ toward $La_{1.25}Ba_{1.75}Mn_2O_7$ preserves the A-cation ordering. Thus, in both the $La_{1.25}Ba_{1.75}Mn_2O_6$ and $La_{1.25}Ba_{1.75}Mn_2O_7$ compounds the rock-salt cation positions are preferentially occupied by the larger Ba^{2+} cations ($r = 1.47$ Å, CN = 9), whereas the smaller La^{3+} cations ($r = 1.20$ Å, CN = 9) are preferentially located in the perovskite block. The resulting $(Ba_{1.75}La_{0.25}O_2)$ composition of the rock-salt block in $La_{1.25}Ba_{1.75}Mn_2O_6$ and $La_{1.25}Ba_{1.75}Mn_2O_7$ results in an expansion of this block in comparison with the rock-salt block in $La_{3.2}Ba_{0.8}Mn_3O_{10}$. This way, the mismatch with the perovskite block is relieved even without the tilting distortion. Note also that the bond valence sums (BVS) for the A-site cations in $La_{3.2}Ba_{0.8}Mn_3O_{10}$ are equal to 2.67(3) and 2.56(2) for the rock-salt and perovskite positions, respectively. Therefore, the coordination environment of the A cations in both blocks is similar, so that the La and Ba cations are disordered and the strains are not relieved by A-site ordering.

The BVS for the Mn cations are close to the formal valence of +2.93, as expected from the chemical composition. The Mn1 cation at the center of the perovskite block appears to be slightly overbonded (BVS = 3.13(1)), whereas the Mn2 cation at the periphery of the perovskite block is slightly underbonded (BVS = 2.86(2)). Both $Mn1O_6$ and $Mn2O_6$ octahedra are deformed because of the elongation of the apical Mn−O bonds. This deformation is imposed by the Jahn−Teller (JT) effect, which is intrinsic in the Mn^{3+} cations. The $Mn2O_6$ are more distorted than the $Mn1O_6$ octahedra as reflected by the octahedral distortion parameter Δd defined as $\Delta d = 1/6\sum_{n=1-6}[(d_n - d)/d]^2$, where d_n is an individual B−X bond length and d is the average B−X bond length ($\Delta d(Mn1O_6) = 1.44 \times 10^{-4}$, $\Delta d(Mn2O_6) = 1.94 \times 10^{-3}$).[19] The apical elongation of the MnO_6 octahedra was also observed in the $n = 2$ RP $La_{1.4}Sr_{1.6}Mn_2O_7$ compound,[20] although in $La_{1.25}Ba_{1.75}Mn_2O_7$ a drastically different apical compression was observed.[18] The authors of ref 16 ascribe the unusual apically compressed JT deformation of the MnO_6 octahedra to the tensile strain of the perovskite block imposed by the large rock-salt block, which is mainly occupied by the Ba cations. Thus, $n = 2$ $La_{1.25}Ba_{1.75}Mn_2O_7$ and $n = 3$ $La_{3.2}Ba_{0.8}Mn_3O_{10}$ show completely different structural behavior: (1) In $La_{1.25}Ba_{1.75}Mn_2O_7$, the perovskite blocks are under tensile strain, which leads to the suppression of the octahedral tilting distortion and triggers the apically compressed JT deformation of the MnO_6 octahedra. (2) In $La_{3.2}Ba_{0.8}Mn_3O_{10}$, the perovskite blocks are under compressive strain that introduces the octahedral tilting distortion and favors the apically elongated JT deformation of the MnO_6 octahedra.

A short remark about the chemical composition and synthesis conditions should also be given. The fact that the variation of the La/Ba ratio, Mn^{2+}/Mn^{3+} ratio, and the annealing temperature did not allow us to get rid of admixture phases may reflect that the $La_{3.2}Ba_{0.8}Mn_3O_{10}$ compound is stabilized in a quite narrow range of partial oxygen pressures only. Thus, the phase composition of the sample will depend not only on the chemical composition of the RP phase, but also on the temperature and sample mass/tube volume ratio that makes it very difficult to find the optimal synthesis conditions. Perhaps annealings at a partial oxygen pressure fixed by a proper getter could be utilized to obtain the phase-pure $n = 3$ RP $(La_{4-x}Ba_x)Mn_3O_{10}$ phase. The preparation of single-phase samples will be instrumental in stimulating future physical studies of layered manganites. For example, the combination of large remnant magnetization and spin freezing observed in $La_{3.2}Ba_{0.8}Mn_3O_{10}$ is notably different from the antiferromagnetic behavior of $n = 1$ RP $LaSrMnO_4$[21,22] and $Sr_2MnO_{3.5}$[23,24] and $n = 2$ RP $YSr_2Mn_2O_{6.54}$,[25] containing Mn in the oxidation state of +3. The Ba-based $n = 1, 2$ RP manganites with Mn^{3+} are also dissimilar to $La_{3.2}Ba_{0.8}Mn_3O_{10}$. For example, $LaBaMnO_4$[21] and $Ln_2BaMn_2O_7$ (Ln = Sm, Eu, Gd, Tb)[26] lack long-range magnetic order down to at least 5 K. This diversity of the magnetic behavior apparently calls for a deeper investigation of the orbital ordering as well as relevant magnetic couplings in the $La_{3.2}Ba_{0.8}Mn_3O_{10}$ compound.

■ ASSOCIATED CONTENT

Ⓢ Supporting Information

Tables with statistics on the extracted PED data. PED patterns used. Details on the PED treatment of the data. This material is available free of charge via the Internet at http://pubs.acs.org.

■ AUTHOR INFORMATION

Corresponding Author

*E-mail: joke.hadermann@ua.ac.be.

Notes

The authors declare no competing financial interest.

■ ACKNOWLEDGMENTS

J.H. acknowledges financial support from the Research Foundation-Flanders (FWO G.0184.09N) and from the University of Antwerp through a BOF-NOI grant. M.G.R. and E.V.A. are grateful to Russian Foundation for Basic Research (Grant 10-03-00992a) for financial support. A.A.T. acknowledges funding by Alexander von Humboldt Foundation and the Mobilitas grant of the ESF.

■ REFERENCES

(1) Moritomo, Y.; Asamitsu, A.; Kuwahara, H.; Tokura, Y. *Nature* **1996**, *380*, 141.

(2) Fawcett, D.; Veith, G. M.; Greenblatt, M.; Croft, M.; Nowik, I. *J. Solid State Chem.* **2000**, *155*, 96−104.

(3) Battle, P. D.; Blundell, S. J.; Coldea, A. I.; Cussen, E. J.; Rosseinsky, M. J.; Singleton, J.; Spring, L. E.; Vente, J. F. *J. Mater. Chem.* **2001**, *11*, 160.

(4) Schaak, R.; Afzal, D.; Schottenfeld, J.; Mallouk, T. *Chem. Mater.* **2002**, *14*, 442.

(5) Chai, P.; Liu, Y.; Liu, X.; Lv, M.; Meng, J. *J. Solid State Chem.* **2010**, *183*, 676.

(6) Battle, P. D.; Green, M. A.; Lago, J.; Millburn, J. E.; Rosseinsky, M. J.; Vente, J. F. *Chem. Mater.* **1998**, *10*, 664.

(7) Sousa, P. M.; Carvalho, M. D.; Melo Jorge, M. E.; Costa, F. M.; Cruz, M. M.; Godinho, M. *Solid State Sci.* **2003**, *5*, 943.

(8) Petricek, V.; Dusek, M. *JANA2000: Programs for Modulated and Composite Crystals*; Institute of Physics: Praha, Czech Republic, 2000.

(9) Aleksandrov, K. S.; Bartolome, J. *Phase Transitions* **2001**, *74*, 255.

(10) Kerman, S.; Campbell, B. J.; Satyavarapu, K. K.; Stokes, H. T.; Perselli, F.; Evans, J. S. O. *Acta Crystallogr.* **2012**, *A68*, 222.

(11) Perez-Mato, J. M.; Orobengoa, D.; Aroyo, M. I.; Elcoro, L. *J. Phys.: Conf. Ser.* **2010**, *226*, 012011.

(12) Campbell, B. J.; Stokes, H. T.; Tanner, D. E.; Hatch, D. M. *J. Appl. Crystallogr.* **2006**, *39*, 607.

(13) Bloch, D.; Feron, J.-L.; Georges, R.; Jacobs, L. S. *J. Appl. Phys.* **1967**, *38*, 1474.

(14) Potter, C. D.; Swiatek, M.; Bader, S. D.; Argyriou, D. N.; Mitchell, J. F.; Miller, D. J.; Hinks, D. G.; Jorgensen, J. D. *Phys. Rev. B* **1998**, *57*, 72.

(15) Moreo, A.; Yunoki, S.; Dagotto, E. *Science* **1999**, *283*, 2034.

(16) Christensen, A. N.; Lebech, B. *Acta Chem. Scand.* **1990**, *44*, 902.

(17) Alonso, J. A.; Amador, J.; Gutierrez-Puebla, E.; Monge, M. A.; Rasines, I.; Ruiz Valero, C. *Solid State Commun.* **1990**, *7*, 1327.

(18) Zurita-Blasco, M. D.; Attidekou, P. S.; Wright, A. J. *J. Mater. Chem.* **2007**, *17*, 923.

(19) Alonso, J. A.; Martínez-Lope, M. J.; Casais, M. T.; Fernández-Díaz, M. T. *Inorg. Chem.* **2000**, *39*, 917.

(20) Argyriou, D. N.; Mitchell, J. F.; Radaelli, P. G.; Bordallo, H. N.; Cox, D. E.; Medarde, M.; Jorgensen, J. D. *Phys. Rev. B* **1999**, *59* (13), 8695.

(21) Bieringer, M.; Greedan, J. E. *J. Mater. Chem.* **2002**, *12*, 279.

(22) Kawano, S.; Achiwa, N.; Kamegashira, N.; Aoki, M. *J. Phys. (Paris)* **1988**, *49*, 829.

(23) Gillie, L. J.; Wright, A. J.; Hadermann, J.; Van Tendeloo, G.; Greaves, C. *J. Solid State Chem.* **2002**, *167*, 145.

(24) Kato, C.; Iikubo, S.; Soda, M.; Sato, M.; Kakurai, K.; Yoshii, S. *J. Phys. Soc. Jpn.* **2005**, *74*, 1026.

(25) Hayward, M. A. *Chem. Mater.* **2006**, *18*, 321.

(26) Shimono, A.; Hayashi, K.; Kamegashira, N. *Mater. Chem. Phys.* **1991**, *28*, 175.